

## Research Article

# Novel 3D instrument navigation in intracranial vascular surgery with multi-source image fusion and self-calibration

Linsen Zhang<sup>a,b</sup>, Shiqi Liu<sup>b,\*</sup>, Xiaoliang Xie<sup>b</sup>, Xiaohu Zhou<sup>b</sup>, Zengguang Hou<sup>b,\*</sup>, Xinkai Qu<sup>c</sup>, Wenzheng Han<sup>c</sup>, Meng Song<sup>b</sup>, Xiyao Ma<sup>b</sup>, Haining Zhao<sup>b</sup>

<sup>a</sup> School of Intelligence Science and Technology, University of Science and Technology Beijing, Beijing 100083, China

<sup>b</sup> Institute of Automation, Chinese Academy of Sciences, Beijing 100190, China

<sup>c</sup> Huadong Hospital Affiliated to Fudan University, Shanghai 200040, China

## ARTICLE INFO

## Article history:

Received 6 January 2025

Revised 9 March 2025

Accepted 29 March 2025

Available online 22 April 2025

## Keywords:

Cerebrovascular interventional surgery

Surgical robot

3D prediction guide

Autonomous instrumentation control

## ABSTRACT

In cerebrovascular interventional surgery, spatial position prediction navigation (SPPN) provides 3D spatial information of the vascular lumen, reducing the spatial dimension loss from digital subtraction angiography (DSA) and improving surgical precision. However, it is limited in its adaptability to complex vascular environments and prone to error accumulation. To address these issues, we propose spatial position prediction-based multimodal navigation (SPPMN), integrating minimal intraoperative X-ray images to enhance SPPN accuracy. In the first phase, a feature-weighted dynamic time warping (FDTW)-based branch matching algorithm is introduced for 3D topological positioning under non-registered conditions, with a dynamic location repositioning module for real-time corrections. In the second phase, an occlusion correction module, based on the elastic potential energy of the instrument tip, dynamically adjusts the tip's angle to achieve low-projection occlusion control. Experimental validation using a high-precision electromagnetic tracking system (EMTS) on a 3D vascular model shows that the proposed method achieves an average 3D positioning accuracy of 9.36 mm in intracranial vascular regions, with a 78% reduction in radiation exposure, significantly enhancing both precision and safety in interventional surgeries.

© 2025 The Author(s). Published by Elsevier B.V. on behalf of Shandong University. This is an open access article under the CC BY-NC-ND license (<http://creativecommons.org/licenses/by-nc-nd/4.0/>).

## 1. Introduction

Cerebrovascular diseases are the second leading cause of death worldwide [1]. Vascular interventional surgery, with its minimal invasiveness and rapid recovery advantages, has become the mainstream approach for treating cerebrovascular diseases [2–4]. Physicians rely on DSA fluoroscopic images in traditional procedures to guide instruments along the vascular lumen to the lesion site and perform treatments based on the lesion type. However, due to the limitations of X-ray imaging, physicians can only approximate the local 2D relative positions of instruments, vessels, and other anatomical features. This makes it challenging to intuitively and accurately understand the 3D information during surgery, resulting in significant reliance on personal experience and judgment [5,6]. Such constraints frequently lead to instrument delivery deviations, causing complications such as vascular rupture or entry into incorrect branch vessels, which can severely endanger the patient's life [7].

3D positioning technology for intravascular instruments significantly enhances surgical quality and reduces the difficulty of surgery, which has attracted widespread attention [8–15]. Current research mainly falls into two categories: projection mapping navigation and magnetic tracking navigation. Projection mapping navigation uses registration algorithms to map the 2D instrument positions from DSA into the 3D model reconstructed from vascular CT scans for display [16]. However, due to the non-visualization of blood vessels, this method requires the maintenance of contrast agent infusion during registration. Additionally, during the procedure, patient movements, such as breathing, heartbeat, and shifts, cause blood vessel positioning changes, significantly affecting the registration results. At the same time, the X-ray radiation during the guiding process significantly increases the health risks for both patients and doctors. Magnetic tracking navigation uses interventional instruments with magnetic positioning capabilities to display the instrument's position and orientation within a registered 3D vascular model [17,18]. While this method demonstrates good positioning results in a fixed vascular environment, patient movements like heartbeat, breathing, and shifts during surgery introduce registration errors. Moreover, the electromagnetic environment requirements and clinical regulatory restrictions also pose challenges to the practical application of this technology.

\* Corresponding authors.

E-mail addresses: [shiqi.liu@ia.ac.cn](mailto:shiqi.liu@ia.ac.cn) (S. Liu), [zengguang.hou@ia.ac.cn](mailto:zengguang.hou@ia.ac.cn) (Z. Hou).

The spatial position prediction navigation (SPPN) based on spatial position prediction localization can achieve millimeter scale 3D positioning of instruments in the main vascular segments without relying on spatial registration and external sensors [19]. This method adopts a multi-stage positioning framework, which includes trajectory prediction, trajectory analysis, and spatial position prediction modules. First, the trajectory prediction module generates all potential trajectories of the instrument based on the vascular robot's delivery feedback data, using a global path planning algorithm on the preoperative computerized tomography (CT) reconstructed 3D vascular model. Then, the trajectory analysis module performs mechanical analysis on the generated trajectories using constraints and a hybrid physical model to filter out invalid trajectories. Finally, the spatial position prediction module statistically analyzes the tip positions of the remaining trajectories using a clustering algorithm and weighted spherical error probable, thereby predicting the most probable position of the instrument tip. This algorithm can achieve precise instrument positioning in the relatively simple aortic vessel structure, but due to the complex topology of cerebrovascular structures, it is susceptible to errors in branch localization during the prediction process.

The spatial position prediction-based multimodal instrument navigation (SPPMN) is based on SPPN and combines with intraoperative X-ray images for real-time correction of instrument position, which can realize 3D guidance of instruments in complex vascular interventions such as cerebrovascular surgery. Given the spatial distribution and scale differences of multi-source instrument trajectories, similarity analysis algorithms are required to extract features from the data across both modalities, enabling position correction of the SPPN-based localization results. The current trajectory similarity evaluation algorithms can be classified into the following types: Euclidean Distance calculates the straight-line distance between trajectory points to assess the similarity between points in space [20]. However, it does not account for the dynamic characteristics of time series, making it ineffective for measuring the similarity of trajectories with different lengths, and it is sensitive to noise points. Cosine Similarity evaluates similarity by computing the cosine of the angle between two trajectories [21]. This method measures the directional similarity of the trajectories but is insensitive to variations in time scale and speed changes. Pearson Correlation Coefficient measures the linear correlation between two trajectories based on their time series, capturing the linear relationship between them [22,23]. However, this method performs poorly for non-linear relationships between trajectories and is susceptible to the influence of outliers. Fréchet Distance considers the shape and temporal synchronization of the trajectories, capturing the shortest distance between the trajectories' contact points [24,25]. However, its high computational complexity limits its real-time applicability. Dynamic Time Warping aligns two trajectories non-linearly, making it robust to local deformations in time series data [26,27]. However, it lacks specific optimization for trajectory direction and outliers.

Furthermore, to improve the accuracy of the SPPMN position correction process, it is necessary to design a reasonable closed-loop instrument control algorithm based on the vascular robot to ensure that the instrument's deformable region in the 2D X-ray images during the procedure is not affected by projection occlusion. Currently, several control methods exist for flexible body structures: Impedance control adjusts the system rigidity by setting impedance parameters, achieving flexible control of elastic instruments. However, this method only controls a single variable and is susceptible to interference in dynamic environments [28,29]. Fuzzy control implements closed-loop control in changing scenarios based on preset control rules. However,

lacking a mathematical model makes it challenging to achieve high-precision operation [30]. Model Predictive Control (MPC) periodically identifies the current state information through a sliding window, optimizing control inputs dynamically. However, its high computational complexity and dependency on external parameters make it challenging to meet the real-time demands in complex scenarios [31]. Based on the Markov Decision Process (MDP), deep reinforcement learning control achieves autonomous instrument delivery using both online and offline operational data. However, its large-scale data training requirements and low interpretability limit its widespread application in clinical and other specific scenarios [32–37].

In summary, our contributions in this work are as follows.

- This paper pioneeringly proposes a spatial position prediction-based multimodal real-time 3D navigation algorithm, enabling millimeter scale vascular intervention instrument guidance with low radiation in cerebrovascular interventions.
- This paper introduces an intraoperative image guidance compensation (IIGC) module based on the proposed FDTW algorithm, which enables trajectory similarity computation across modalities without registration, thereby achieving real-time correction of the predicted 3D trajectory position.
- This paper presents a state-feedback-based adaptive closed-loop control (SACC) algorithm. By dynamically adjusting the angle of the instrument tip's shaping segment, it effectively reduces projection occlusion under 2D X-ray.
- This paper quantitatively validates the system's performance in a real patient's scale-model 3D soft gel model.

## 2. Methodology

Fig. 1 shows the proposed SPPMN system framework. The system utilizes a serial structure composed of the SPPN and IIGC modules to achieve 3D spatial localization based on preoperative CT images and dynamically calibrates the 3D localization results through the timely fusion of intraoperative 2D images. This section will sequentially introduce the details of the SPPN module, as well as the components and functions of the IIGC module.

### 2.1. SPPN

SPPN is based on a preoperative CTA 3D reconstruction model and achieves real-time localization of the instrument tip in 3D space by capturing the displacement and rotation angle of the instrument during the operation of the vascular robot [19]. As shown in Fig. 1, it adopts a three-stage sequential framework comprising three modules: trajectory prediction, trajectory analysis, and spatial position estimation.

The trajectory prediction module employs a global path planning algorithm based on DC-A\*, using delivery displacement and the 3D trajectory curvature  $Cur_{max}$  as constraints to generate all potential instrument trajectories under the current delivery displacement. Compared with traditional algorithms such as A\*, DC-A\* integrates vascular centerline and vessel size information, allowing dynamic adjustments of planning speed and direction based on vascular characteristics, thereby achieving superior path planning performance. Here,  $G(i)$  represents the current trajectory cost,  $d(i)$  denotes the maximum inscribed circle diameter at the current position, and  $H_c$  refers to the hybrid terminal distance.

Next, the trajectory analysis module addresses standard vascular interventional instruments' segmented bending and torsional deformation characteristics by developing a hybrid physical model based on 1R-PRB and Cosserat-rods. This model simulates both motion states and establishes a mapping between the

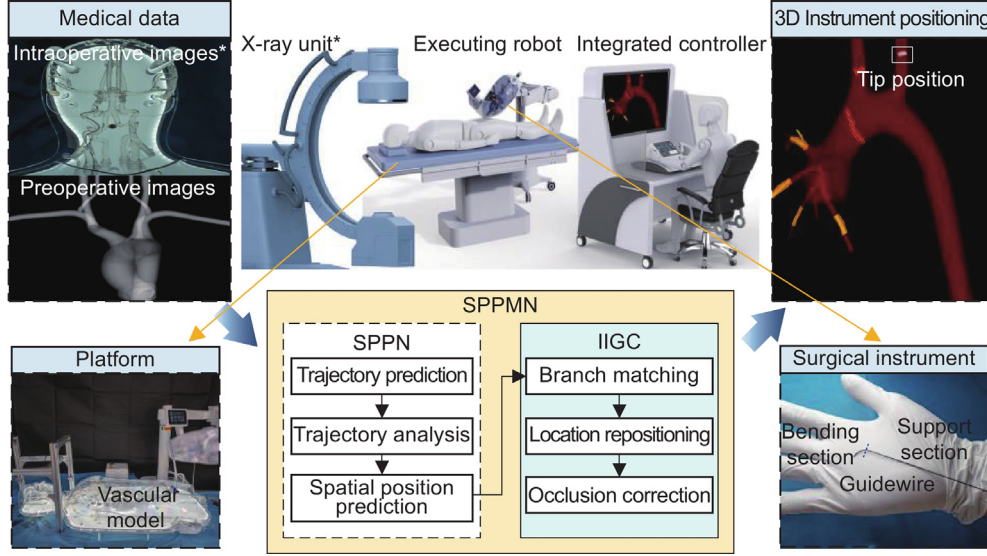


Fig. 1. Framework diagram of SPPMN-based 3D real-time instrument navigation.

### Algorithm 1 Trajectory generation algorithm

**Input:** Vascular 3D environment, step-size  $\rho(i)$ , point  $Y(i)$ , delivery distance  $dis$ , direction vectors  $V_i$

**Output:** Trajectory set

**while**  $\min(G(i)) \leq dis$  **do**

```

     $i = \arg \min G(i)$ 
     $\rho(i) = \frac{d(i)}{A}$ 
     $OP = \rho(i) \times V_i$ 
    for Each in OP do
         $NewNode = Y(i) + OP$ 
        if  $NewNode$  inside the blood vessel then
            if  $Cur(i) \leq Cur_{max}$  then
                Calculate  $H_c(i)$  and  $G(i)$ , store trajectory
            else
                Delete trajectory
            end
        end
    end
end

```

**end**

instrument's morphology and mechanical properties. In particular, a trajectory feature point extraction algorithm is designed to optimize data efficiency. This method significantly reduces the overall data volume without removing any individual trajectory.

Finally, the spatial position estimation module predicts the most probable position of the instrument tip based on the previously computed planning and model information. This module first employs the density-based spatial clustering of applications with noise algorithm (DBSCAN) to classify the point cloud data of the instrument tip, segmenting the raw unstructured point cloud into multiple sets representing different states. Then, it integrates multi-parameter prior knowledge from each point set to determine the highest probability set. Subsequently, a weighted probability error sphere is applied to conduct the final statistical analysis of this set, enabling precise prediction of the instrument's most probable distribution region, which is then output as the final result.

### 2.2. Branch matching

This subsection aims to achieve 3D localization of vascular branches by performing topological analysis to match the intraoperative 2D trajectory of the instrument tip with its 3D trajectory from the SPPN.

The DSA system provides the 2D intraoperative instrument trajectory, and its external structure is shown in Fig. 2. The system consists of the imaging system and the c-arm. The imaging system, composed of the X-ray generator and flat panel detector, is fixed on the c-arm. By adjusting the imaging system's angle in three directions, the physician can view fluoroscopic images from different angles during the procedure.

First, we need to project the 3D instrument trajectory  $S_{3d}(i)$  onto a 2D plane for correlation analysis between the 2D trajectories.

$$S_{3d}(i) = (x(i), y(i), z(i)) \quad (1)$$

Considering that variations in the X-ray projection angle ( $\theta_x$ ,  $\theta_y$ , and  $\theta_z$ ) may lead to affine transformations, we dynamically adjust  $S_{3d}(i)$  based on the three-axis angles to achieve alignment of the projection plane.

$$R = R_z(\theta_z) \cdot R_y(\theta_y) \cdot R_x(\theta_x) \quad (2)$$

$$R_x(\theta_x) = \begin{bmatrix} 1 & 0 & 0 \\ 0 & \cos(\theta_x) & -\sin(\theta_x) \\ 0 & \sin(\theta_x) & \cos(\theta_x) \end{bmatrix} \quad (3)$$

$$R_y(\theta_y) = \begin{bmatrix} \cos(\theta_y) & 0 & \sin(\theta_y) \\ 0 & 1 & 0 \\ -\sin(\theta_y) & 0 & \cos(\theta_y) \end{bmatrix} \quad (4)$$

$$R_z(\theta_z) = \begin{bmatrix} \cos(\theta_z) & -\sin(\theta_z) & 0 \\ \sin(\theta_z) & \cos(\theta_z) & 0 \\ 0 & 0 & 1 \end{bmatrix} \quad (5)$$

The mapped 2D trajectory  $S(i)$  is shown in the following equation.

$$S(i) = (R \cdot S_{3d}(i))_{xy} \quad (6)$$

After achieving alignment of the projection angles, the spatial positions of the two trajectories need to be unified. To this end,

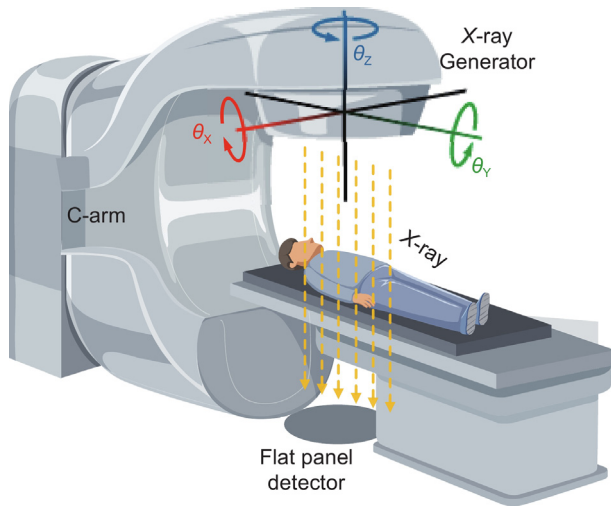


**Fig. 2.** Schematic diagram of a C-arm driven DSA fluoroscopy machine. The X-ray generator and flat panel detector can dynamically adjust their angles in three directions.

we extract  $n$  points with the highest curvature from both trajectories to perform spatial alignment based on feature information.

$$S_{\text{top}n} = \{S(i) \mid i \in \text{Top}n(\kappa)\} \quad (7)$$

$$P_{\text{top}n} = \{P_{2d}(i) \mid i \in \text{Top}n(\kappa)\} \quad (8)$$

$S_{\text{top}n}$  and  $P_{\text{top}n}$  represent the sequences of the top  $n$  points with the highest curvature values from the trajectory  $S(i)$  and the intraoperative 2D trajectory  $P_{2d}(i)$ , respectively.  $\text{Top}n(\kappa)$  denotes the indices of the top  $n$  points with the highest curvature values.

After adjusting the spatial scale, the trajectories of  $S(i)$  and  $P_{2d}(i)$  are accurately aligned. As shown in Eq. (9), the mean alignment error between the feature point sets  $S_{\text{top}n}$  and  $P_{\text{top}n}$  is first calculated and used as the translation vector  $t$ . Then, the translation vector  $t$  is applied to shift  $P_{2d}(i)$  in order to minimize the alignment error  $E(t)$ .

$$t = [t_x, t_y]^T = \frac{1}{n} \sum_{i=1}^n [S_{\text{top}(i)} - P_{\text{top}(i)}]^T \quad (9)$$

$$E(t) = \sum_{k=1}^n \|S_{\text{top}(k)} + t - P_{\text{top}(k)}\|^2 \quad (10)$$

To better achieve the correlation analysis between the trajectories, we unified the head and tail lengths  $L_1$  and  $L_2$  of the different trajectories to improve alignment accuracy.

$$L_1 = \sum_{k=1}^{i_1-1} \|S(k+1) - S(k)\| \quad (11)$$

$$L_n = \sum_{k=i_n}^{N-1} \|S(k+1) - S(k)\| \quad (12)$$

Here,  $i_1$  and  $i_n$  represent the indices of the trajectory points whose distances from the head and tail feature points of the trajectory  $S(i)$  are  $L_1$  and  $L_n$ , respectively. Trajectory points beyond this range will be removed.

To further improve the alignment accuracy of trajectories with lower unidirectional feature information, we designed the FDTW algorithm, which integrates vascular curvature information  $Cur$

and vascular diameter constraint  $D$  at the nodes.

$$d_{DTW^*}(S, P) = \min_{\varphi, \psi} \sum_{i=1}^m \sum_{j=1}^n w(i, j) \cdot d(S(i), P(i)) \quad (13)$$

Here,  $d(S(i), P(i))$  represents the euclidean distance between the nodes.  $\lambda_1$  is the correction factor, set to 5.  $m$  and  $n$  represent the number of nodes in the trajectories  $S(i)$  and  $P(i)$ , respectively.  $D(i)$  represents the vessel diameter at the position of the  $i$ th point in trajectory  $S(i)$  in the 3D vascular scene.

$$w(i, j) = \frac{1}{1 + \lambda_1 \cdot |Cur(S(i)) - Cur(P(j))|} \quad (14)$$

$$d(S(i), P(i)) = \begin{cases} \infty, & d(S(i), P(i)) > D(i) \\ d(S(i), P(i)), & d(S(i), P(i)) \leq D(i) \end{cases} \quad (15)$$

Ultimately, the branch with the smallest trajectory correlation distance  $d_{\min}$  will be identified as the target branch, enabling dynamic matching of the 3D vascular branches. The pseudocode of the algorithm in this section is shown in Algorithm 2.

#### Algorithm 2 Branch matching algorithm based on FDTW

```

1: Input:  $\{S_{3d}(1), S_{3d}(2), \dots, S_{3d}(k)\}$  {Set of  $k$  3D instrument trajectory}
2: Input:  $P$  {2D instrument intraoperative trajectory}
3: Input:  $\lambda$  {Curvature weighting parameter}
4: Input:  $D_i$  {Distance threshold}
5: Minimum distance  $d_{\min} \leftarrow \infty$ 
6: best_match_index  $\leftarrow -1$ 
7: for  $i = 1$  to  $k$  do
8:   Step 1: Projection Angle Alignment
9:   Project  $S_{3d}(i)$  to 2D using  $R$ 
10:  Step 2: Feature Position Alignment
11:  Adjust the spatial scale of  $P_{2d}(i)$  to match  $S_{3d}(i)$ 
12:  Extract top  $n$  curvature points from  $S(i)$  and  $P_{2d}(i)$ 
13:  Compute  $\mathbf{t} = [t_x, t_y]$ 
14:  Apply translation to  $P_{2d}(i)$  (get  $P(i)$ )
15:  Step 3: Correlation calculation
16:  Trim the start and end of  $S(i)$  and  $P(i)$  using  $L_1$  and  $L_2$ 
17:  Initialize the cost matrix  $d_{DTW^*}$  of size  $m \times n$ 
18:  Set the initial condition:  $d_{DTW^*}(0, 0) \leftarrow 0$ 
19:  for  $j = 1$  to  $m$  do
20:    for  $l = 1$  to  $n$  do
21:      Compute the weighted distance  $w(i, j)$  based on curvature
22:      Compute the Euclidean distance  $d(S(i), P(i))$ 
23:      Update  $d_{DTW^*}$ :  $d_{DTW^*}(j, l) \leftarrow \min(d_{DTW^*}(j-1, l), d_{DTW^*}(j, l-1), d_{DTW^*}(j-1, l-1)) + w(i, j) \cdot d(S(i), P(i))$ 
24:    end for
25:  end for
26:  Extract the final distance from  $d_{DTW^*}(m, n)$ 
27:  if  $d_{DTW^*}(m, n) < d_{\min}$  then
28:    Update  $d_{\min} \leftarrow d_{DTW^*}(m, n)$ 
29:    Update best_match_index  $\leftarrow i$  {Best match trajectory index}
30:  end if
31: end for
32: Output: best_match_index
33: Output:  $d_{\min}$ 

```

As shown in Fig. 3, subfigures a to d illustrate the results of the branch matching module's serial operation. Specifically, in subfigure c, the two-dimensional intraoperative X-ray instrument trajectory, after curvature feature point extraction, is dynamically matched with the curvature feature points of the two-dimensional trajectory projected from the original three-

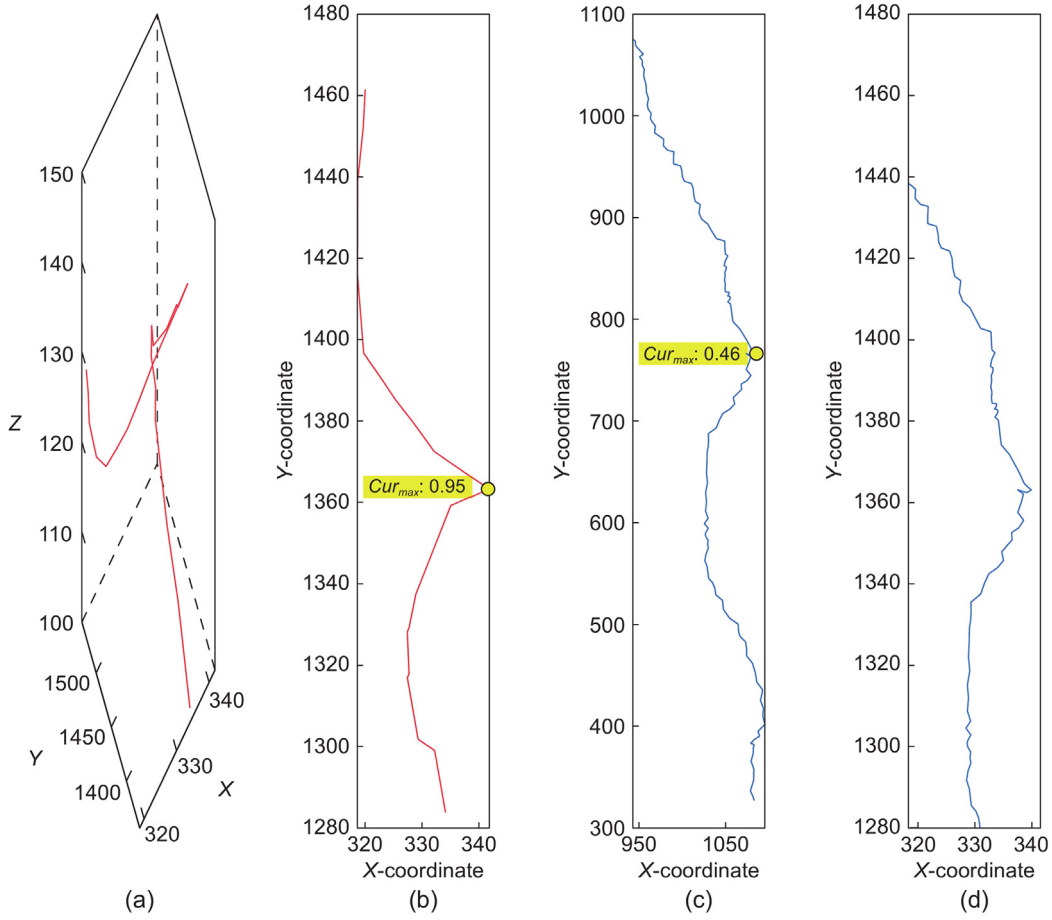


**Fig. 3.** Schematic plot of the branch matching process.(a) Original 3D instrument positioning trajectory; (b) Projection of the 3D trajectory onto the 2D guidance plane; (c) Original 2D real-time guidance trajectory; (d) 2D real-time guidance trajectory after feature matching.

dimensional SPPN trajectory in subfigure b. The aligned two-dimensional intraoperative X-ray trajectory is shown in subfigure d. In both subfigures b and c,  $Cur_{max}$  represents the point with the maximum curvature value in  $S_{topn}$  and  $P_{topn}$ , which is used to demonstrate the trajectory alignment effect.

### 2.3. Location repositioning

After achieving dynamic matching of the vascular branches, this subsection will utilize the real-time intraoperative 2D instrument position to correct the SPPN localization results, enabling location repositioning.

Firstly, as shown in the following equation, the 3D centerline trajectory node, projected onto the 2D plane, that is closest to the current real-time position  $P(i)$  of the instrument is matched.

$$j_i = \arg \min_j (\|P_{2D}(i) - S_{cen}(j)\|) \quad (16)$$

$$d_{3D}(S(i), S_{cen}(j_i)) = \sqrt{(s'_x - s_x)^2 + (s'_y - s_y)^2} \quad (17)$$

Next, using the current 3D position  $S(i)$  and the 3D centerline node  $S_{cen}(j_i)$  matched to the 2D real-time position, the unit error vector  $\hat{v}(i)$  between the two is computed.

$$\hat{v}(i) = \frac{S_{cen}(j_i) - S(i)}{\|S_{cen}(j_i) - S(i)\|} \quad (18)$$

Finally, using a suitable correction parameter  $\lambda_2$  and the error distance between the paired nodes, the corrected 3D instrument

real-time position  $S'(i)$  is given by the following equation. Here,  $\lambda_2$  is set to a conventional value of 0.7.

$$S'(i) = S(i) + \lambda_2 \cdot d_{3D}(S(i), S_{cen}(j_i)) \cdot \hat{v}(i) \quad (19)$$

### 2.4. Occlusion correction

This subsection designs the SACC algorithm based on the instrument's bending potential energy, aiming to avoid position recognition errors caused by the 2D projection occlusion of the instrument tip's deformable region, thereby improving the accuracy of the 3D guidance.

The curved section (i.e., the shaping section) is located at the anterior end of the guidewire and is pre-shaped into a specific arc before the procedure to optimize its adaptability for entering different vascular branches. As shown in Fig. 1, this section, together with the support section, forms the fundamental structure of a conventional vascular interventional guidewire.

As shown below, we first trim the head-end nodes of the 2D real-time trajectory, which consists of  $h$  points, so that its total length  $L_{total}$  is approximately equal to the length of the instrument's plastic segment.

$$P(s) = (x_s, y_s), \quad s \in 1, 2, \dots, h \quad (20)$$

$$L_{total} = \sum_{s=1}^{h-1} |P(s+1) - P(s)| \quad (21)$$

Next, we calculate the straight-line distance  $L_0$  between the start and end points of the 2D head-end trajectory to assess the

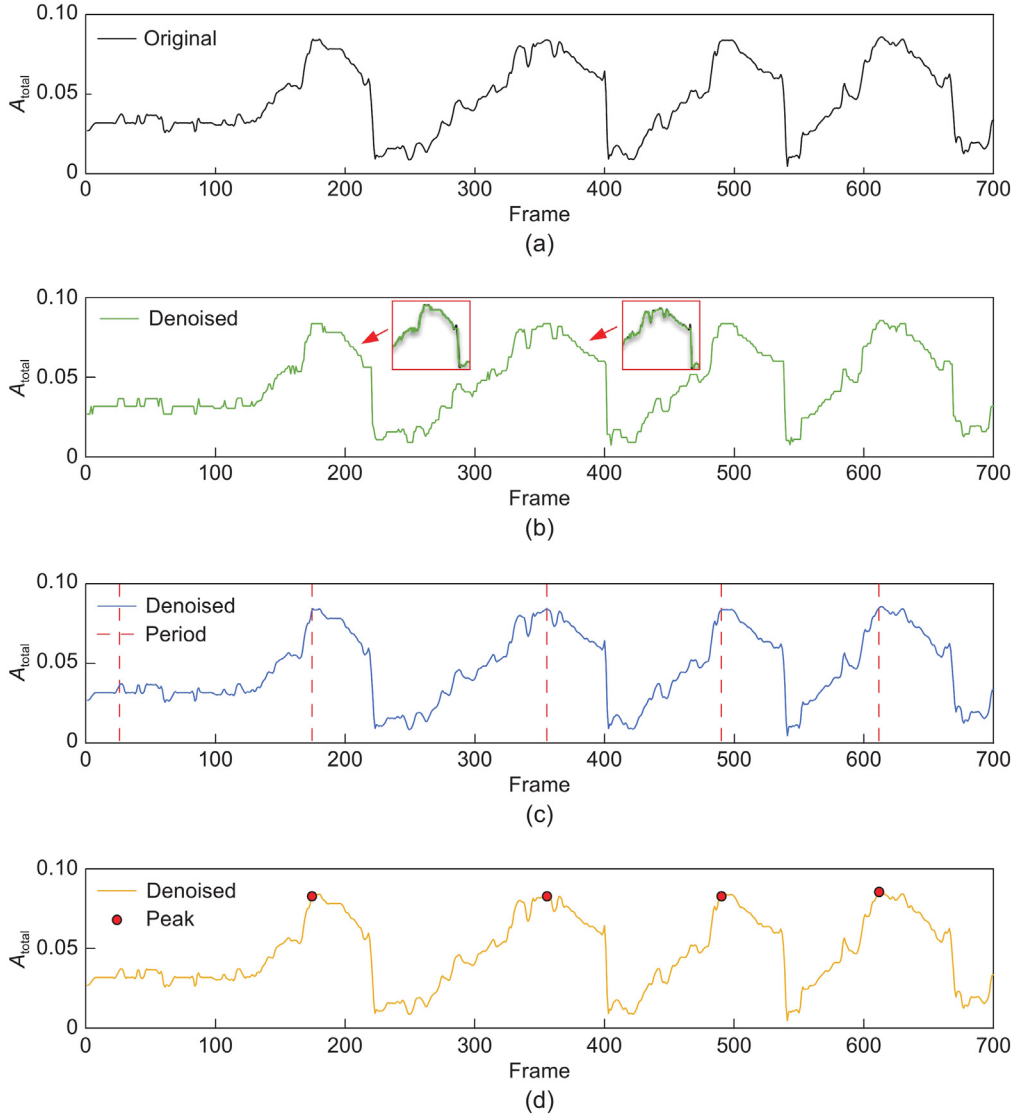


**Fig. 4.** Plot of trajectory elastic potential energy data analysis. (a) Original data; (b) Data after wavelet filtering; (c) Periodic analysis results; (d) Peak detection results.

bending potential energy of the trajectory.

$$L_0 = |P(h) - P(1)| \quad (22)$$

The bending elastic potential energy  $A_{total}$  of the trajectory based on the elastic rod is given by Eq. (23), where  $\alpha$  is a linear adjustment factor, set to 1 here [38,39].  $L_{total}$  is the total length of the elastic rod, calculated by summing the distances between the discretized nodes.

$$A_{total} = \alpha \cdot (L_{total} - L_0)^2 \quad (23)$$

Subsequently, as shown in Fig. 4, this subsection conducts a two-stage data acquisition and analysis of the elastic potential energy of the plastic segment trajectory under constant-speed rotation of the instrument. In the first stage, we apply wavelet transform to decompose the original signal into multiple scales, remove high-frequency noise at higher scales, and then reconstruct the original signal. In the second stage, the signal's period  $T$  is calculated using a peak detection algorithm to analyze the signal's periodicity and peak value  $A_{max}$ .

Considering the known errors in the signal period  $T$  and peak value  $A_{max}$  of elastic potential energy, this subsection designs a multi-parameter state feedback control strategy. By controlling the instrument's directional rotation, the strategy aims to maximize the elastic potential energy, ensuring the complete display of the tip's plastic region.

The state vector can be represented as

$$x[k] = \begin{bmatrix} \Delta\phi[k] \\ \Delta A[k] \end{bmatrix} \quad (24)$$

The control input  $u[k]$  is applied to minimize the phase error  $\Delta\phi[k]$  and the peak error  $\Delta A[k]$ . The state feedback gain parameters  $k_\phi$  and  $k_A$  are designed with a three-segment approach and are dynamically adjusted based on  $\Delta\phi[k]$  and  $\Delta A[k]$ , respectively. Specifically, the control law is defined as follows:

$$\begin{aligned} u[k] &= -Kx[k] \\ &= - \begin{bmatrix} k_\phi & k_A \end{bmatrix} \begin{bmatrix} \Delta\phi[k] \\ \Delta A[k] \end{bmatrix} \end{aligned} \quad (25)$$

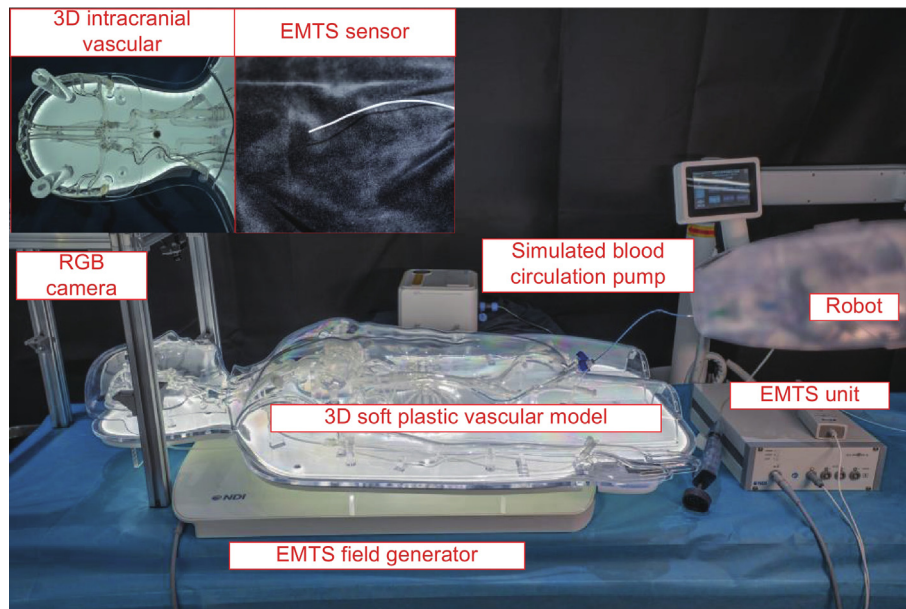


Fig. 5. 3D human vascular model experimental scene diagram.

### 3. Experimental settings

This section addresses clinical needs by designing and constructing an experimental verification platform based on an actual patient's 3D full-body vascular model and an EMTS to quantitatively validate the positioning accuracy and control performance of robot-assisted instrumenting delivery under SPPMN guidance.

#### 3.1. Experimental environment

##### 3.1.1. Vascular robot

The vascular surgery robot in this study adopts a master–slave structure, where the slave execution mechanism is driven via the master-end control system over a network. The execution mechanism delivers or rotates the guidewire using two clamping roller motors, with these actions achieved through forward–backward rotation or longitudinal relative movement. During delivery, the maximum error is 0.38 mm [19]. Within the typical control speed range, the maximum longitudinal delivery error of the instrument is 0.24 mm, and the maximum retraction error is 0.38 mm [19]. The execution mechanism operates at a specified speed and can provide real-time feedback on its current operating state.

##### 3.1.2. Experiment preparation

The system operates in a Windows 10 environment with an Intel(R) Core(TM) i7-10700 CPU. To minimize the impact of external light reflection, internal light refraction, and low texture contrast during visible light observation, a transparent model optical imaging environment, as shown in Fig. 5, was constructed to enhance the image signal-to-noise ratio. In the experiment, the NDI-Aurora EMTS was selected as the reference for the instrument's spatial position, with real-time data acquisition via serial communication. The system's positioning accuracy is 1.1 mm, with a maximum measurement frequency of 40 Hz. The visible light camera on top captures high-contrast trajectories of the dark instrument, simulating the instrument's X-ray image results. The instrument used in the experiment is a standard hydrophilic membrane guidewire commonly used in intracranial interventional surgeries, with a length of 190 cm and a diameter of 0.035 inches.

##### 3.1.3. EMTS space registration

Since the coordinate systems and scales of EMTS and SPPMN differ, a 3D scaling transformation and spatial registration are required. To achieve this, we applied the normal distribution transform (NDT) algorithm, using EMTS to sequentially collect the coordinates of 20 marker points on the external model and match them with the corresponding coordinates in the SPPMN [40]. The points were then processed using least squares iteration to improve the registration accuracy. After registration, the average error between the two systems was 0.93 mm, with a maximum error of 1.46 mm.

#### 3.2. Implementation details

##### 3.2.1. Spatial positioning accuracy experiment

This experiment aims to evaluate the accuracy of the 3D positioning of the SPPMN system during intracranial vascular intervention procedures. The experimental area covers common surgical vascular regions from the common iliac artery to the intracranial arteries. As shown in Fig. 5, the tracking probe of the EMTS is fixed at the tip of the intervention instrument to collect real-time position reference values. The initial position of the instrument is set at the bifurcation of the common iliac artery, a location with distinct anatomical features, while the target position is the middle section of the six intracranial arteries shown in Fig. 6. The initial position of the instrument was corrected by the EMTS system, ensuring that the positional error in the delivery direction is controlled within 2 mm. Simulated blood with density and viscosity is similar to real blood, and a blood circulation pump is used to replicate hemodynamic conditions better and simulate the real vascular environment. During the experiment, the surgical robot autonomously operates the instrument with periodic delivery intervals of 10 mm, thus enabling a smooth evaluation of the positioning error in the vascular region. Each group of experiments is repeated five times.

##### 3.2.2. Instrument angle control accuracy experiment

After evaluating the spatial positioning accuracy, we quantitatively assessed the autonomous angle control function of the instrument shaping segment implemented by the occlusion correction module. During the experiment, the instrument tip was

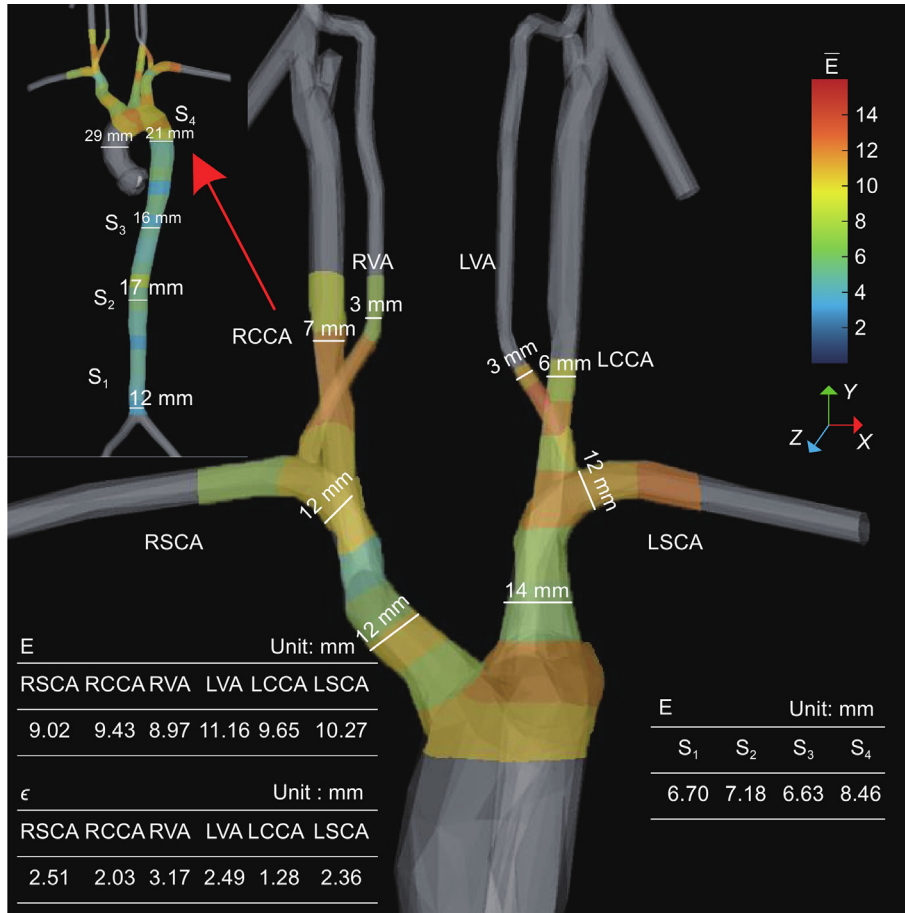


Fig. 6. Plot of the 3D instrument localization error under multiple regions.

Table 1 Table of multi-algorithm branch matching results.

| Method      | Accuracy      | $R_{sim}$   |
|-------------|---------------|-------------|
| Euclidean   | 33.33%        | 0.72        |
| Cosine      | 16.67%        | 0.39        |
| Pearson     | 33.33%        | 0.01        |
| Frechet     | 33.33%        | 0.40        |
| DTW         | 50.00%        | 0.24        |
| <b>Ours</b> | <b>83.33%</b> | <b>0.61</b> |

Table 2 Ablation experiment results of the FDTW algorithm. (PA and CC denote whether the feature position alignment and correlation calculation modules are enabled, respectively).

| Method | PA | CC | Accuracy      | $R_{sim}$   |
|--------|----|----|---------------|-------------|
| FDTW   | -  | -  | 16.67%        | 0.15        |
|        | ✓  | -  | 16.67%        | 0.20        |
|        | -  | ✓  | 50.00%        | 0.43        |
|        | ✓  | ✓  | <b>83.33%</b> | <b>0.61</b> |

placed in the unobstructed camera regions of the middle sections of the six intracranial arteries shown in Fig. 6 to improve the signal-to-noise ratio. The elastic potential setting value was set to 0.8 times the signal peak value  $A_{max}$  to ensure better the stability of the control process and the system's robustness. Each group of experiments was repeated five times for different vascular regions.

#### 4. Results and discussion

##### 4.1. Guidance performance results

The spatial positioning accuracy experiment results quantified the positioning accuracy of SPPMN, demonstrating that the

Table 3 Table of ANOVA results for different directions of 3D navigation.

| Catalog       | df  | MS     | F           | P-value     | Fcrit |
|---------------|-----|--------|-------------|-------------|-------|
| MSB(X)        | 4   | 161.19 | 1.29        | 0.27        | 2.40  |
| MSE(X)        | 240 | 124.31 | -           | -           | -     |
| MSB(Y)        | 4   | 4.94   | <b>0.04</b> | <b>0.99</b> | 2.40  |
| <b>MSE(Y)</b> | 240 | 123.32 | -           | -           | -     |
| MSB(Z)        | 4   | 703.39 | 1.14        | 0.34        | 2.40  |
| MSE(Z)        | 240 | 616.38 | -           | -           | -     |

SPPMN system can achieve millimeter scale spatial positioning accuracy in both aortic and intracranial vascular interventions. As shown in Fig. 6, we divided the proximal and middle segments of the aorta and intracranial vessels into several sections according

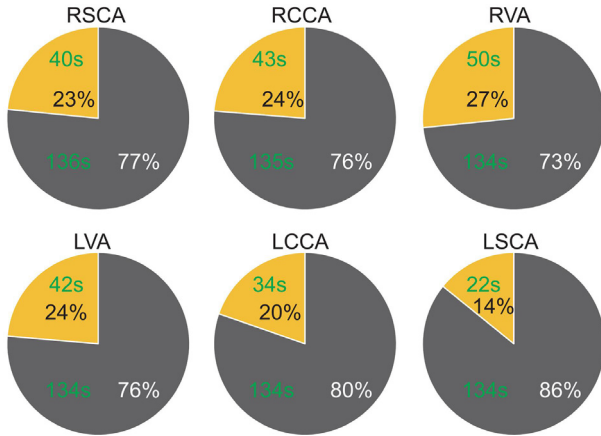


**Fig. 7.** Pie chart of the X-ray dependent area (camera-on) proportion under SPPMN guidance in different intracranial vascular branch surgeries. The yellow area represents X-ray dependency, and the gray area represents X-ray-free guidance. The green numbers represent the average time, respectively.

to their anatomical structure. The average spatial localization error of SPPMN in the aortic vessel region (i.e., from S1 to S4) is 6.01 mm, with an average spatial localization error of 2.43 mm in the delivery direction.

$$R_{sim} = \frac{|R_i - \bar{R}|}{R_{max} - R_{min}} \quad (26)$$

Subsequently, after manually placing the catheter, we quantitatively evaluated the branch match performance for six intracranial vascular branches shown in the figure. As shown in Table 1, we compared our method with five common trajectory similarity measurement algorithms. To better analyze the algorithm's ability to distinguish correct trajectories, we proposed the dissimilarity ratio parameter  $R_{sim}$ , which can be applied to any monotonic evaluation function. The results show that the proposed FDTW algorithm outperforms existing algorithms in accuracy and  $R_{sim}$ , demonstrating superior trajectory matching performance.

To evaluate the performance gains of the feature position alignment and correlation calculation modules in the FDTW algorithm, an ablation study was conducted. As shown in Table 2, with the gradual activation of the feature position alignment and correlation calculation modules, both the branch matching accuracy and the dissimilarity ratio  $R_{sim}$  of the FDTW algorithm improve. When both modules are enabled simultaneously, the algorithm achieves optimal performance.

Furthermore, we evaluated the guidance accuracy for each intracranial vascular branch. The average spatial localization error of the six major intracranial vascular branches is 9.75 mm, while the average spatial localization error along the delivery direction is 5.62 mm. Compared to the smoother aorta, the narrow and tortuous intracranial vessels caused frequent irregular deformations of the instrument tip, which in turn reduced the prediction accuracy to some extent. Additionally, we compared the positioning accuracy optimization effects before and after enabling location repositioning. The average 3D positioning accuracy improvement  $\epsilon$  for each branch was 2.30 mm, with the RVA vascular branch, which underwent more significant deformation, achieving the highest optimization effect, with an improvement of 3.17 mm.

At the same time, in this task, the positioning accuracy of projection mapping and EMTS navigation under ideal laboratory conditions is approximately 2 mm, which is superior to SPPMN. However, both are limited by registration issues in the complex surgical environment, such as patient breathing, heartbeat, and movement, as well as the increased size of the instruments. In contrast, SPPMN can achieve greater guiding robustness in clinical scenarios using conventional instruments.

To validate the variance in the EMTS three-axis data, we performed an Analysis of Variance (ANOVA). In Table 3, X, Y, and Z represent the data in the three directions. MSB and MSE denote the between-group and within-group variances, respectively. The results show that the MSB for the X and Z axes is significantly larger than the MSE, with a  $P$ -value far smaller than 0.05. In contrast, the MSB for the Y-axis is much smaller than the MSE, with a  $P$ -value greater than 0.95. This indicates that the data in the X and Z axes exhibit large between-group differences, suggesting that the instrument tip's positioning along the X and Z axes is highly random.

Finally, this subsection presents a statistical analysis of the X-ray dependency area, precisely the proportion of the range required for the RGB camera to be activated, as shown in Fig. 5. As shown in Fig. 7, compared to traditional X-ray guidance, SPPMN significantly reduces radiation time in six common intracranial vascular branch surgeries, with an average reduction of 134.5 s and an average decrease rate of 78%.

#### 4.2. Instrument operation performance results

The quantitative control results of instrument angles in multiple intracranial vascular branches demonstrate the superiority of the autonomous control system. Fig. 8 shows that the instrument angle closed-loop control in all six vascular branches achieved stable closure. Using elastic potential energy as the evaluation criterion, the mean absolute error (MAE) was 0.001, and the mean relative error (MRE) was 2.20%. The experimental results confirm that the Occlusion Correction module can effectively realize the automatic quantitative rotation control of the instrument tip, reducing projection occlusion in the plastic region.

### 5. Conclusion

This paper proposes a spatial position prediction-based multimodal navigation system (SPPMN), which enables low X-ray radiation exposure, 3D millimeter scale instrument guidance, and autonomous control during intracranial vascular intervention surgeries. In the initial implementation of SPPMN, the proposed IIGC module performs non-registered feature analysis on intraoperative real-time images and 3D predicted trajectories, enabling dynamic matching of vascular branches and repositioning of the instrument tip. Subsequently, through closed-loop control for the quantitative rotation of the instrument tip, the projection occlusion of the instrument's plastic segment is reduced, further improving the guidance accuracy of SPPMN. Additionally, we quantitatively validate the guidance and instrument control performance of SPPMN on a scaled 3D soft gel vascular model of real clinical patients.

Our future research will focus on two main areas. First, we plan to analyze the impact of hemodynamics and vascular elastic deformation on instrument guidance to improve the positioning accuracy further. Second, we will design comparative experiments and conduct validation on animal models to assess the system's performance and reliability in a real biological environment.

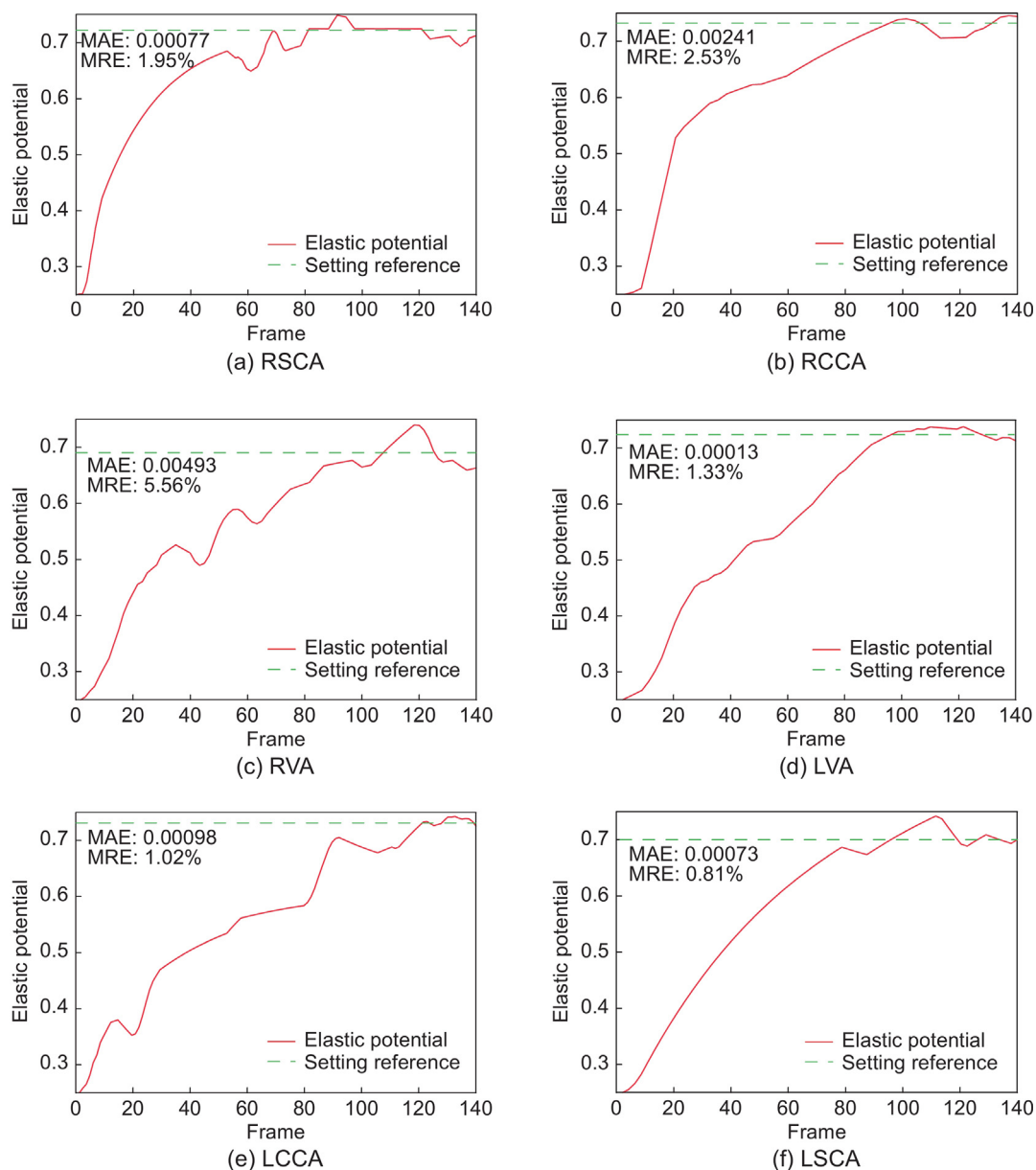


Fig. 8. Plot of experimental results for instrument angle autonomous control in different intracranial vascular branches.

### CRedit authorship contribution statement

**Linsen Zhang:** Writing – review & editing, Writing – original draft, Visualization, Validation, Methodology, Investigation, Data curation. **Shiqi Liu:** Writing – review & editing. **Xiaoliang Xie:** Writing – review & editing. **Xiaohu Zhou:** Writing – review & editing. **Zengguang Hou:** Supervision. **Xinkai Qu:** Investigation. **Wenzheng Han:** Investigation. **Meng Song:** Investigation. **Xiyao Ma:** Writing – review & editing. **Haining Zhao:** Writing – review & editing.

### Declaration of competing interest

The authors declare that they have no known competing financial interests or personal relationships that could have appeared to influence the work reported in this paper.

### Acknowledgments

This work was supported in part by the National Key Research and Development Program of China (2024YFF1206902); in part by the National Natural Science Foundation of China (62303463); in part by the Beijing Natural Science Foundation, China (L232137, L246047); in part by the National High Level Hospital Clinical Research Funding (2022-PUMCH-B-125).

### Appendix A

The following are the abbreviations used in the text. Right Subclavian Artery (RSCA), Right Common Carotid Artery (RCCA), Right Vertebral Artery (RVA), Left Vertebral Artery (LVA), Left Common Carotid Artery (LCCA), Left Subclavian Artery (LSCA).

### Appendix B. Supplementary data

Supplementary material related to this article can be found online at <https://doi.org/10.1016/j.birob.2025.100233>.

## References

- [1] GBD 2019 Stroke Collaborators, Global, regional, and national burden of stroke and its risk factors, 1990–2019: A systematic analysis for the Global Burden of Disease Study 2019, *Lancet Neurol.* 20 (10) (2021) 795.
- [2] H.S. Oh, et al., Stent-assisted coil embolization versus flow-diverting stent in unruptured vertebral artery dissecting aneurysms: Efficacy and safety comparison, *Neurosurgery* 93 (1) (2023) 120–127.
- [3] H. Li, X. Zhou, X. Xie, S. Liu, Z. Feng, Z. Hou, CASOG: Conservative actor-critic with SmOoth gradient for skill learning in robot-assisted intervention, *IEEE Trans. Ind. Electron.* 71 (7) (2024) 7725–7734.
- [4] H. Li, X. Zhou, X. Xie, S. Liu, Z. Feng, M. Gui, T. Xiang, D. Huang, Z. Hou, Model-based offline reinforcement learning for autonomous delivery of guidewire, *IEEE Trans. Med. Robot. Bionics* 6 (3) (2024) 1054–1062.
- [5] R. Gupta, et al., Robotic vs manual percutaneous coronary intervention - boon or a bane? *J. Am. Coll. Cardiol.* 77 (18\_Supplement\_1) (2021) 1024–1024.
- [6] L.W. Klein, et al., SCAI multi-society position statement on occupational health hazards of the catheterization laboratory: Shifting the paradigm for healthcare workers' protection, *J. Am. Coll. Cardiol.* 75 (14) (2020) 1718–1724.
- [7] Y. Sandoval, M.R. Bell, R. Gulati, Transradial artery access complications, *Circ.: Cardiovasc. Interv.* 12 (11) (2019) e007386.
- [8] R. Abadía-Heredia, A. Pariente, J.M. Pérez, S.L. Clainche, Tortuosity in tumours: The need of combining multi-phase flows with machine learning tools, *Results Eng.* 11 (2021) 100234.
- [9] X.-Y. Wei, F. Ju, H. Guo, B. Chen, H.-T. Wu, Modeling and control of cable-driven continuum robot used for minimally invasive surgery, *J. Eng. Med.* 237 (1) (2023) 35–48.
- [10] S.D. Olson, S. Lim, R. Cortez, Modeling the dynamics of an elastic rod with intrinsic curvature and twist using a regularized Stokes formulation, *J. Comput. Phys.* 238 (2013) 169–187.
- [11] Z.-J. Wang, M. Fratarcangeli, A. Ruimi, A.R. Srinivasa, Real time simulation of inextensible surgical thread using a Kirchhoff rod model with force output for haptic feedback applications, *Int. J. Solids Struct.* 113 (2017) 192–208.
- [12] M.J. Eagleton, Updates in endovascular procedural navigation, *Can. J. Cardiol.* 38 (5) (2022) 662–671.
- [13] J. Burgner-Kahrs, D.C. Rucker, H. Choset, Continuum robots for medical applications: A survey, *IEEE Trans. Robot.* 31 (6) (2015) 1261–1280.
- [14] J.-L. Wang, S. Song, L. Liu, Editorial for the special issue on design, sensing and control in medical robots, *Biomim. Intell. Robot.* 4 (3) (2024) 100177.
- [15] W.-N. Chen, et al., A survey of autonomous robots and multi-robot navigation: Perception, planning and collaboration, *Biomim. Intell. Robot.* 5 (2) (2025) 100203.
- [16] R. Schaffert, J. Wang, P. Fischer, A. Borsdorf, A. Maier, Learning an attention model for robust 2-D/3-D registration using point-to-plane correspondences, *IEEE Trans. Med. Imaging* 39 (10) (2020) 3159–3174.
- [17] A.M. Franz, et al., Electromagnetic tracking in medicine—a review of technology, validation, and applications, *IEEE Trans. Med. Imaging* 33 (8) (2014) 1702–1725.
- [18] S. Sharma, et al., Wireless 3D surgical navigation and tracking system with 100 $\mu$ m accuracy using magnetic-field gradient-based localization, *IEEE Trans. Med. Imaging* 40 (8) (2021) 2066–2079.
- [19] L.-S. Zhang, et al., A novel spatial position prediction navigation system makes surgery more accurate, *IEEE Trans. Med. Imaging* 42 (12) (2023) 3614–3624.
- [20] P. Han, J. Wang, D. Yao, S. Shang, X.-L. Zhang, A graph-based approach for trajectory similarity computation in spatial networks, in: *ACM SIGKDD Conference on Knowledge Discovery & Data Mining*, 2021, pp. 556–564.
- [21] P.-R. Tong, M.-Q. Li, M. Li, J.-Q. Huang, X.-S. Hua, Large-scale vehicle trajectory reconstruction with camera sensing network, in: *Annual International Conference on Mobile Computing and Networking*, 2021, pp. 188–200.
- [22] G.-Z. Peng, D. Xu, J.-H. Zhou, Q. Yang, W.-M. Shen, A novel curve pattern recognition framework for hot-rolling slab camber, *IEEE Trans. Ind. Inform.* 19 (2) (2023) 1270–1278.
- [23] D.-W. Xu, X.-T. Shang, H. Peng, H.-J. Li, MVHGN: Multi-view adaptive hierarchical spatial graph convolution network based trajectory prediction for heterogeneous traffic-agents, *IEEE Trans. Intell. Transp. Syst.* 24 (6) (2023) 6217–6226.
- [24] D. lei Hu, et al., Spatio-temporal trajectory similarity measures: A comprehensive survey and quantitative study, *IEEE Trans. Knowl. Data Eng.* 36 (5) (2024) 2191–2212.
- [25] G. Joachim, S.M. P., W. Sampson, Map matching queries on realistic input graphs under the Fréchet distance, *ACM Trans. Algorithms* 20 (2) (2024) 1549–6325.
- [26] B. Taha, Y. Yan, D.J. Rao, Dynamic time warping based adversarial framework for time-series domain, *IEEE Trans. Pattern Anal. Mach. Intell.* 45 (6) (2023) 7353–7366.
- [27] C.-Y. Shuai, et al., Intelligent diagnosis of abnormal charging for electric bicycles based on improved dynamic time warping, *IEEE Trans. Ind. Electron.* 70 (7) (2023) 7280–7289.
- [28] Z. Liu, et al., An autonomous guidewire delivery method with distal position-based impedance control, *IEEE Trans. Autom. Sci. Eng.* (2024) 1–15.
- [29] L.-L. Chen, P.-Y. Lai, Y.-L. Wang, Y.-X. Dong, Fuzzy adaptive variable impedance control on deformable shield of defecation smart care robot, *Biomim. Intell. Robot.* (2025) 100214.
- [30] N.-E. Li, Y.-W. Wang, H. Zhao, H. Ding, Robotic systems design in endovascular treatment, *IEEE Trans. Med. Robot. Bionics* 6 (2) (2024) 367–383.
- [31] L.-S. Zhang, et al., An improved networked predictive controller for vascular robot using 5g networks, in: *2021 43rd Annual International Conference of the IEEE Engineering in Medicine & Biology Society, EMBC*, 2021, pp. 4674–4678.
- [32] L. Karstensen, et al., Learning-based autonomous vascular guidewire navigation without human demonstration in the venous system of a porcine liver, *Int. J. Comput. Assist. Radiol. Surg.* 17 (11) (2022) 2033–2040.
- [33] W.-Q. Chi, et al., Collaborative robot-assisted endovascular catheterization with generative adversarial imitation learning, in: *IEEE International Conference on Robotics and Automation*, 2020, pp. 2414–2420.
- [34] A. Pore, et al., Autonomous navigation for robot-assisted intraluminal and endovascular procedures: A systematic review, *IEEE Trans. Robot.* 39 (4) (2023) 2529–2548.
- [35] H. li, et al., Model-based offline reinforcement learning for autonomous delivery of guidewire, *IEEE Trans. Med. Robot. Bionics* 6 (3) (2024) 1054–1062.
- [36] W.-Q. Chi, et al., Trajectory optimization of robot-assisted endovascular catheterization with reinforcement learning, in: *IEEE/RSJ International Conference on Intelligent Robots and Systems*, 2018, pp. 3875–3881.
- [37] H. Alcaraz-Herrera, M.-A. Tsompanas, I. Balaz, A. Adamatzky, Using neuroevolution for designing soft medical devices, *Biomim. Intell. Robot.* 5 (1) (2025) 100205.
- [38] A.A. Nazari, F. Janabi-Sharifi, K. Zareinia, Image-based force estimation in medical applications: A review, *IEEE Sensors J.* 21 (7) (2021) 8805–8830.
- [39] A.A. Alqumsan, S. Khoo, M. Norton, Robust control of continuum robots using Cosserat rod theory, *Mech. Mach. Theory* 131 (2019) 48–61.
- [40] Z.-C. Zhou, et al., NDT-transformer: Large-scale 3D point cloud localisation using the normal distribution transform representation, in: *2021 IEEE International Conference on Robotics and Automation, ICRA*, 2021, pp. 5654–5660.